3-D positioning and target association for medium resolution SAR sensors

Dheenathayalan, Prabu; Small, David; Hanssen, Ramon

DOI
10.1109/TGRS.2018.2844108

Publication date
2018

Document Version
Final published version

Published in
IEEE Transactions on Geoscience and Remote Sensing

3-D Positioning and Target Association for Medium-Resolution SAR Sensors

Prabu Dheenathayalan, *Member, IEEE*, David Small, *Member, IEEE*, and Ramon F. Hanssen, *Senior Member, IEEE*

***Abstract*— Associating a radar scatterer to a physical object is crucial for the correct interpretation of interferometric synthetic aperture radar measurements. Yet, especially for medium-resolution imagery, this is notoriously difficult and dependent on the accurate 3-D positioning of the scatterers. Here, we investigate the 3-D positioning capabilities of ENVISAT medium-resolution data. We find that the data are perturbed by range-and-epoch-dependent timing errors and calibration offsets. Calibration offsets are estimated to be about 1.58 m in azimuth and 2.84 m in range and should be added to ASAR products to improve geometric calibration. The timing errors involve a bistatic offset, atmospheric path delay, solid earth tides, and local oscillator drift. This way, we achieve an unbiased positioning capability in 2-D, while in 3-D, a scatterer was located at a distance of 28 cm from the true location. 3-D precision is now expressed as an error ellipsoid in local coordinates. Using the Bhattacharyya metric, we associate radar scatterers to real-world objects. Interpreting deformation of individual infrastructure is shown to be feasible for this type of medium-resolution data.**

***Index Terms*— 3-D accuracy, ENVISAT, error ellipsoid, geocoding, geolocation, infrastructure monitoring, medium resolution, positioning, synthetic aperture radar (SAR), target association.**

I. Introduction

INTERFEROMETRIC synthetic aperture radar (InSAR) is used to measure the earth's topography and surface deformation with a high spatial and temporal sampling. Since the identification of phase-coherent pixels [1]–[3], persistent scatterer interferometry (PSI) was introduced to extract information from a set of scatterers subject to negligible geometrical and temporal decorrelation called PSs [4], [5]. PSI is well applicable to reflections from man-made objects, such as civil infrastructure. However, complications arise in linking radar reflections (PS) to specific objects (or locations on objects) on the ground in order to unambiguously interpret the estimated line-of-sight (LOS) deformation. Here, we attempt to improve the geodetic capacity of PS for infrastructure monitoring using medium-resolution SAR imagery. In our analysis, we assume that the SAR resolution cells contain one dominant scatterer.

Manuscript received March 14, 2017; revised October 16, 2017 and March 27, 2018; accepted May 31, 2018. This work was supported by Liander through the TU Delft project, Monitoring Surface Movement in Urban Areas Using Satellite Remote Sensing. *(Corresponding author: Prabu Dheenathayalan.)*

P. Dheenathayalan and R. F. Hanssen are with the Department of Geoscience and Remote Sensing, Delft University of Technology, 2628 CN Delft, The Netherlands (e-mail: p.dheenathayalan@tudelft.nl).

D. Small is with Remote Sensing Laboratories, University of Zürich, 8057 Zürich, Switzerland.

Color versions of one or more of the figures in this paper are available online at http://ieeexplore.ieee.org.

Digital Object Identifier 10.1109/TGRS.2018.2844108

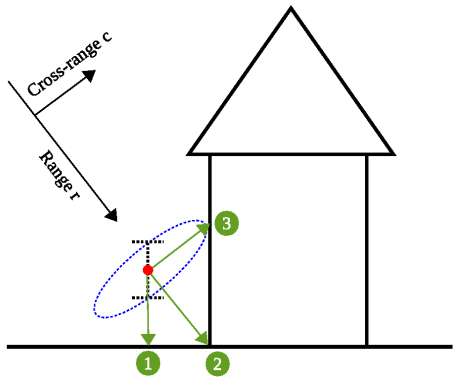

Fig. 1. Linking a scatterer (red dot) to ① ground, ② curb-to-wall interface, or ③ building facade. A cross section of the confidence (error) ellipsoid in the range/cross-range plane is shown in blue dotted circle. The azimuth (flight) direction is perpendicular to the plane. The scatterer height error is shown in black dotted line. In this case, the scatterer is linked to the facade ③ based on the error ellipsoid, instead of the position with the shortest Euclidean distance (or by using only height) ① or the position in the radar look-direction ②.

Associating PS to infrastructure has recently gained more attention, especially using high-resolution sensors, such as TerraSAR-X (TSX) or COSMO-SkyMed. Centimeter-level 2-D (radar coordinates) positioning accuracy was successfully demonstrated using corner reflectors (CRs) in very high-resolution TSX satellite images (see [6], [7]). Ray-tracing was applied to simulate geometric scattering and was helpful in the interpretation of TSX spotlight SAR images [8]. PS was geometrically registered to buildings in a city model with 3-D terrestrial coordinates. Factors influencing PS density, such as surface structure, shadowing, aspect dependence, and quasi-random effects, were discussed in [9]. A systematic procedure to fix positioning errors in radar coordinates, i.e., before geocoding to avoid nonlinear distortions in the 3-D terrestrial coordinates, was proposed [10]–[12]. This procedure results in a high positioning quality and can link the phase center of a radar scatterer to an object (see Fig. 1). This was demonstrated using a TSX stripmap data set in [12]. In [13] and [14], stereo-SAR radar acquisitions were used from multiple tracks to obtain precise 3-D geodetic coordinates of scatterers. However, this approach is not always possible, as: 1) often only one track with time series is available and 2) it requires the same physical scatterer to be visible in both imaging geometries, which is unlikely aside from isolated poles. In contrast to high-resolution SAR imagery, medium- and low-resolution variants feature wide swaths, large volumes of archived imagery, cover a larger area per resolution cell and

TABLE I

IMPACT OF ERROR IN RADAR COORDINATES (r, a, c) ON THE LOCAL COORDINATES (e, n, h) OF A TARGET WITH A LOCAL INCIDENCE ANGLE θ_{inc} AND HEADING ANGLE α_h

	$\kappa = r$	$\kappa = a$	$\kappa = c$
$\frac{\partial e}{\partial \kappa}$	$\cos(\alpha_h)\sin(\theta_{\text{inc}})$	$\sin(\alpha_h)$	$\cos(\alpha_h)\cos(\theta_{\text{inc}})$
$\frac{\partial n}{\partial \kappa}$	$-\sin(\alpha_h)\sin(\theta_{\text{inc}})$	$\cos(\alpha_h)$	$-\sin(\alpha_h)\cos(\theta_{\text{inc}})$
$\frac{\partial h}{\partial \kappa}$	$-\cos(\theta_{\text{inc}})$	0	$\sin(\theta_{\text{inc}})$

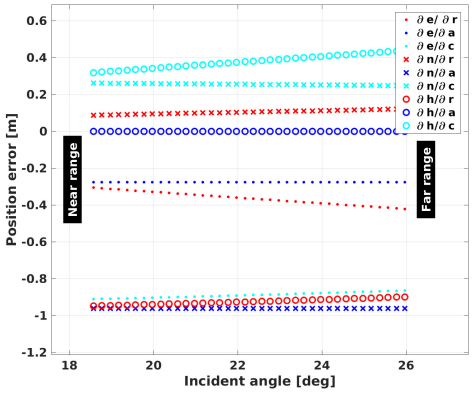

Fig. 2. Nonlinear variation of position error in local coordinates (e, n, h) across the scene for a constant-and-unit change in (r, a, c) when applied to Table I. Here, θ_{inc} variation represents a typical ASAR IMS (Imaging Mode SLC) scene; a heading of $\alpha_h = 196°$ was used.

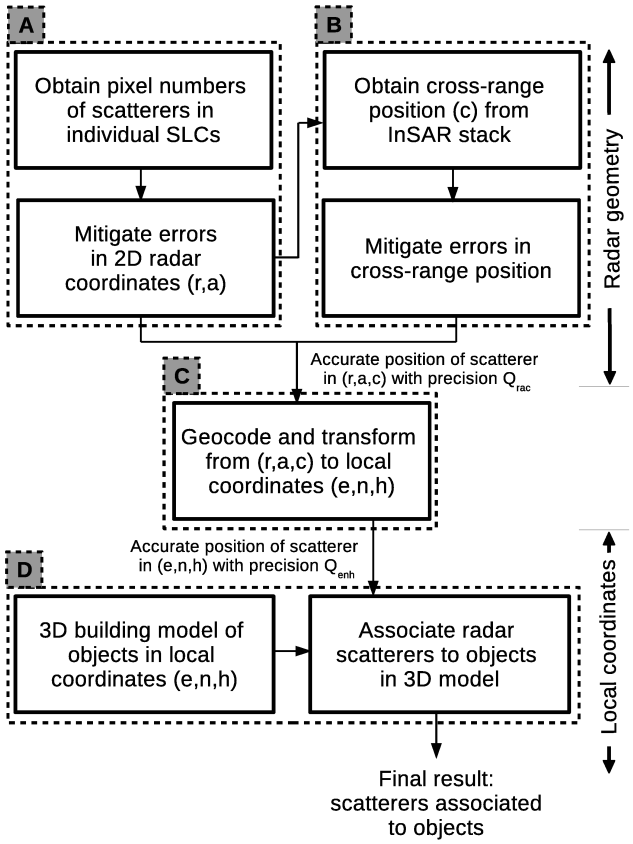

Fig. 3. Procedure to obtain an accurate 3-D position and perform target association to an object.

yield a relatively poor point density. This makes interpretation of coherent scatterers difficult and hampers the monitoring of individual objects.

Scatterer positions in the radar coordinates azimuth a, range r,[1] and cross range c are converted to terrestrial coordinates by a nonlinear transformation known as geocoding [15], [16]. The terrestrial coordinates are converted to local coordinates east e, north n, and height h by a datum transformation. As a result, a constant shift in radar coordinates (a, r, c) will translate into a varying shift in local coordinates (e, n, h). The influence of range, azimuth, and cross range on the local coordinates depends on the local incidence angle θ_{inc} and the heading angle α_h (see Table I and Fig. 2). Due to the large scene extent in medium- and low-resolution imagery, a variety of radar timing offsets (in range and azimuth) further distort the positioning capability. Therefore, a systematic procedure needs to be applied, per scatterer, before applying a geocoding procedure to achieve precise positioning to aid interpretation. The procedure proposed by [12] is studied here for the medium-resolution case, using ENVISAT ASAR data as an example. Although the ENVISAT sensor has stopped acquiring new data after 10 years, ASAR C-band imagery is still widely being processed to understand the geodynamic changes of the Earth during the period from 2002 to 2012 and can serve as an example for other medium-resolution sensors, such as ERS-1/2, RADARSAT-2, and Sentinel-1A/1B.

In this paper, Section II is devoted to the 3-D radar scatterer positioning, its dominant error sources, and linking scatterers to real-world objects. The experimental setup and the positioning results are described in Section III for CRs and other coherent scatterers. Section IV draws the main conclusions.

II. POSITIONING AND TARGET ASSOCIATION

A 2-D SAR image with range and azimuth coordinates (r, a) shows scatterers with (local) 3-D coordinates (e, n, h). Transforming the position of the scatterer from radar geometry to local coordinates, and subsequently linking it to objects, is performed in four steps (see Sections II-A–II-D and Fig. 3).

A. Mitigate Errors in 2-D Position of Radar Scatterers

The position of a radar scatterer P in 2-D radar coordinates (a_P and r_P) is measured by performing complex fast Fourier transform (FFT) oversampling and detecting the subpixel location of its amplitude peak. Thus, the 2-D position in radar coordinates can be obtained solely from a single look complex (SLC) image. The stronger the scatterer's signal-to-clutter ratio (SCR), the smaller its variance in position, $\sigma^2_{r_P}$ and $\sigma^2_{a_P}$.

The 2-D position of a scatterer P in radar coordinates (r_P, a_P) follows from:

$$\begin{aligned} r_P &= \frac{v_0}{2}(\tau_0 + \mu_P(\Delta\tau + \tau_{\text{lo}}) + \tau_{pd_P} + \tau_{\text{set}_P} + \tau_{\text{tect}}) + r_{\text{cal}} \\ a_P &= v_{\text{f/p}}(t_0 + \nu_P(\Delta t + t_{\text{lo}}) + t_{\text{bi}_P} + t_{\text{set}_P} + t_{\text{tect}}) + a_{\text{cal}} \end{aligned} \quad (1)$$

[1]Range always refers to the slant-range radar imaging coordinate, unless explicitly stated otherwise.

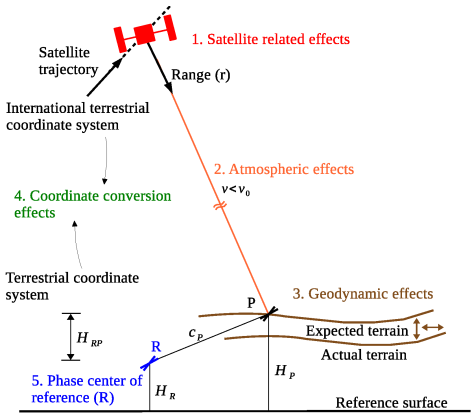

Fig. 4. Components (1–5) impacting scatterer positioning. H_R and H_P are the respective heights of reference point R and target P from a reference surface. H_{RP} and c_P are the height and cross-range position of scatterer P relative to reference point R, respectively. v is the actual propagation velocity of the radio waves between the radar antenna and the scatterer, while v_0 is the velocity in vacuum.

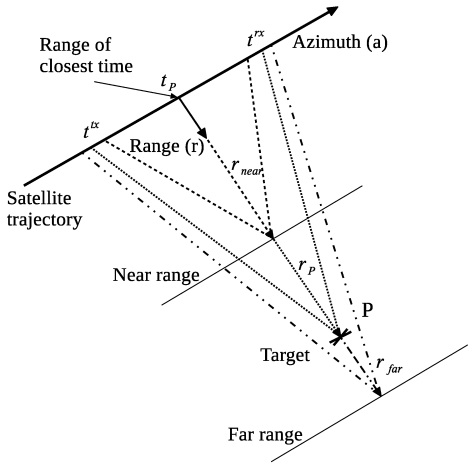

Fig. 5. Bistatic effect scales with the range of the target r_P from the sensor at zero-Doppler (range of closest) time. r_{near} and r_{far} are the distances to the near- and far-range swath extremes.

where

v_0	velocity of microwaves in vacuum;
$v_{\text{f/p}}$	radar beam footprint ground velocity;
t_0	time of transmission of first pulse of focused image;
τ_0	time to the first range pixel;
$\Delta\tau$	range sampling interval;
Δt	azimuth pulse repetition interval;
t_{lo} and τ_{lo}	corrections applied to Δt and $\Delta\tau$ due to local oscillator (LO) drift;
τ_{set_P} and t_{set_P}	timing correction factors due to solid earth tides (SETs) in range and azimuth, respectively;
τ_{tect} and t_{tect}	corrections due to plate tectonics, in range and azimuth, respectively;
τ_{pd_P}	range path delay;
t_{bi_P}	azimuth bistatic correction;
r_{cal} and a_{cal}	residual unmodeled calibration offsets.

These last offsets are unmodeled and need to be empirically estimated and removed during calibration campaigns. While they are location- and epoch-independent, they are sensor-dependent.

In the following, we elaborate on the various components in (1) (see also Fig. 4), subdivided in four classes:

1) satellite-related timing corrections (τ_{lo}, t_{lo}, and t_{bi_P}) (see Section II-A1);
2) atmospheric (τ_{pd_P}) and geodynamic (τ_{set_P} and t_{set_P}) corrections (see Section II-A2);
3) coordinate transformation effects (τ_{tect} and t_{tect}) (see [12]);
4) unmodeled calibration offsets (r_{cal} and a_{cal}) (see Section II-A3).

1) Satellite Corrections: Here, we discuss the impact of three factors: the target-specific bistatic timing correction (t_{bi_P}), the sensor LO drift (τ_{lo} and t_{lo}), and the center-of-mass (CoM) changes of the satellite during its lifetime.

The raw radar signal is transmitted at t^{tx} and recorded at the time of reception t^{rx} of the backscattered (echo) return from the target P (see Fig. 5). During SAR image focusing, the received time of the echo should be converted to zero-Doppler time, i.e., t_P. If this time difference [see t_{bi_P} in (1)] is not compensated for, the azimuth timing error leads to a geolocation shift in azimuth. Note that this azimuth timing error scales proportionally with range (see Fig. 5) between r_{near} and r_{far}. This problem was observed in ENVISAT ASAR data and is known as the "bistatic" effect (see [17]). The bistatic azimuth offset varies between ~18.5 m in near range and ~19.5 m in far range (see Figs. 5 and 10). Though this azimuth bias is strictly an annotation convention issue, it has to be compensated for to achieve optimal positioning accuracy.

Reference [18] reported a systematic frequency decay over the lifetime of the ENVISAT ASAR instrument, which was assumed to originate from the deterioration of the LO performance over time. The LO could introduce a systematic drift in the range position of about 0.04 pixels per year [18]. Hence, the range position can drift about 3 m over the 10 years lifetime of the mission. Based on an analysis over a set of ~10 000 ASAR images, the impact of the LO drift expressed in parts per million was given by [18]

$$\text{LO}_{\text{drift}} = \left[0.7037 + 0.3266\Delta t - 0.01481\Delta t^2 + 0.00348\Delta t^3\right] \cdot 10^{-6} \quad (2)$$

where Δt is the relative time of acquisition in years since January 1, 2008. Here, the constant term in (2) is obtained after removing the calibration offsets from (1) in [18]. Based on (2), a new set of azimuth and range timing parameters [$\Delta\tau + \tau_{\text{lo}}$ and $\Delta t + t_{\text{lo}}$ in (1)] are to be replaced with their corresponding annotated values in the header files to mitigate the effect of this drift.

It is expected that the CoM of the satellite changes during the 10-year ENVISAT mission due to the consumption of fuel (hydrazine). This could cause a drift over time in azimuth and/or range coordinates. Unfortunately, no information could

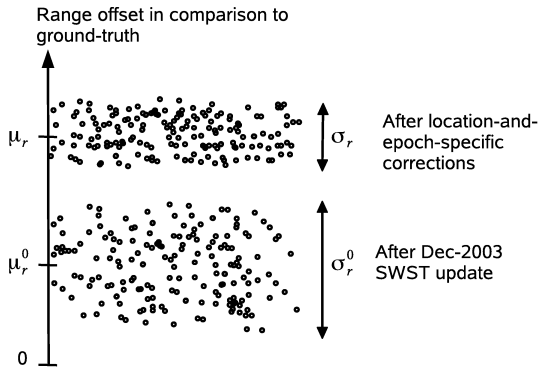

Fig. 6. Expected impact of location- and-epoch-specific corrections (μ_r, σ_r) over a one-time SWST bias range update (μ_r^0, σ_r^0) for ASAR range position.

be retrieved to model this behavior. Here, we assume that the effects of CoM changes will be absorbed implicitly by the other drift corrections.

2) Atmospheric and Geodynamic Effects: Radio waves are delayed by the Earth's ionosphere and the troposphere [19]. This delay is caused by a reduced propagation velocity of the radio waves ($v < v_0$) and the bending of the ray path due to refraction. The latter is negligible for SAR acquisitions with $\theta_{\text{inc}} < 87°$ [20]. Hence, the change in propagation velocity is the only factor attributed to the atmospheric delay.

In the case of the TerraSAR-X satellite, average ionospheric and tropospheric time delays are specifically annotated,[2] enabling users to decide on a tailor made atmospheric correction [22]. In the case of ASAR, such specific annotations are lacking. During the ENVISAT commissioning phase, a mean range position offset (dominated by atmospheric effects) was computed from several calibration targets [transponders (TRs) and CRs] located at several locations (Flevoland, The Netherlands and Dübendorf, Switzerland). This offset was subsequently absorbed in an update of the sampling window start time (SWST) for all ASAR products from December 12, 2003 onward [23]. Thus, instead of annotating all individual corrections, as in TerraSAR-X, ASAR has many physical effects lumped together in one parameter, through which they are not easily separable. These involve timing, atmospheric (ionosphere + troposphere), geodynamic (SET, and so on), and tectonic plate motion effects. Moreover, these values are only based on the situation at a few specific locations and times of the calibration campaign. As the atmospheric delay at the time of the calibration is already lumped in the SWST, doing another full atmospheric correction for a specific location and epoch means that effectively the dominant part of the atmospheric delay will be added again to the data. Thus, it will introduce an increased range position offset, from μ_r^0 to μ_r, as shown in Fig. 6. However, location-and-epoch-specific corrections will decrease the dispersion of the offsets, i.e., the standard deviation decreases from σ_r^0 to σ_r (see Fig. 6). A similar explanation holds for the azimuth position.

3) Empirical Estimation of Residual 2-D Offsets: After removing the modeled corrections in (1), unmodeled offsets r_{cal} and a_{cal} in range and azimuth positions remain. In range, r_{cal} is attributed to a residual internal electronic instrument delay (after internal instrument calibration based upon calibration pulses), the state vector estimation inaccuracies, and range bias between near-field calibration measurements made on the ground prelaunch and actual end-to-end far-field measurements made over calibration site(s) during commissioning. In azimuth, a_{cal} is associated with a potential bias between the ASAR instrument radar time and the time coordinate used in the Doppler orbitography and radio-positioning integrated by satellite orbit determination. These residual offsets, assumed to be common and constant for all ASAR products, need to be estimated using calibration targets. These calibration constants can be considered as a refinement to the December 2003 SWST bias update (r_{cal} for range) and a_{cal} as an additional offset in azimuth. For this purpose, calibration targets, such as CRs or TRs, need to be deployed in the scene, and their ground-truth position needs to be measured using an independent technique. Empirically estimated calibration offsets and precisions in azimuth $(a_{\text{cal}}, \sigma_a)$ and range $(r_{\text{cal}}, \sigma_r)$ are given by

$$\hat{a}_{\text{cal}} = E\{\underline{a}_{i,T} - \underline{a}_{i,E}\} \tag{3}$$

$$\sigma_a^2 = D\{\underline{a}_{i,T} - \underline{a}_{i,E}\} \tag{4}$$

$$\hat{r}_{\text{cal}} = E\{\underline{r}_{i,T} - \underline{r}_{i,E}\} \tag{5}$$

$$\sigma_r^2 = D\{\underline{r}_{i,T} - \underline{r}_{i,E}\} \tag{6}$$

where $E\{\cdot\}$, and $D\{\cdot\}$ are the expectation and dispersion operators, respectively. The underline (e.g., $\underline{r}_{i,T}$ and $\underline{a}_{i,E}$) denotes that the quantities are stochastic in nature. $\underline{a}_E$ and $\underline{r}_E$ are the measured azimuth and range positions of a scatterer in the ith SLC image after correcting for model errors, such as bistatic effect, LO drift, path delay, SET, and plate tectonics. The 3-D ground-truth position of a scatterer is radar-coded by range-Doppler positioning to obtain 2-D radar coordinates $\underline{a}_{i,T}$ and $\underline{r}_{i,T}$ in the ith SLC image [16], [24].

B. Cross-Range Positioning of Radar Scatterers

In order to find the position of a scatterer in 3-D, namely cross range c_P, the interferometric phase is exploited. Unlike azimuth and range, the cross-range component is estimated using a series of interferometric SAR acquisitions in a relative manner, *i.e.*, with respect to a reference point R at a reference epoch (master image) [25]

$$c_P = r_P \cdot \theta_{PR} \tag{7}$$

where θ_{PR} is the change in look angle estimated from PSI. The precision in cross range (σ_{c_P}) is dictated by the phase quality driven by SCR, the perpendicular baseline distribution of the stack, the error in baseline due to orbits, the phase unwrapping (assumed to be error-free), and the precise position of reference point R. The precision of the cross-range position can be written by

$$\sigma_{c_P}^2 = \sigma_{c_{P,\text{orb}}}^2 + \sigma_{c_{P,\text{SCR}}}^2 + \sigma_{c_R}^2 \tag{8}$$

where the terms $\sigma_{c_{P,\text{orb}}}^2$, $\sigma_{c_{P,\text{SCR}}}^2$, and $\sigma_{c_R}^2$ are explained in Sections II-B1--II-B3, respectively.

[2]In the *GEOREF.xml* file.

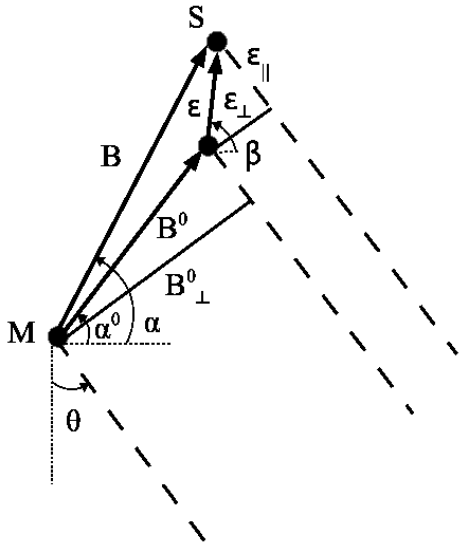

Fig. 7. Propagation of orbit errors to baseline errors. $B(B^0+\mathcal{E})$ and $B_\perp(B_\perp^0+\mathcal{E}_\perp)$ are the baseline and perpendicular baseline with orbit error $\mathcal{E}$, respectively, between a master M and slave S acquisitions. $\mathcal{E}_\perp$ and $\mathcal{E}_\parallel$ are the residual perpendicular and parallel baseline error components, respectively. α is the orientation angle of baseline B. β is the orientation of orbit error $\mathcal{E}$. Superscript zero indicates the corresponding values without taking the error in the state vector ($\mathcal{E}$) into account.

1) Impact of Orbits: The change in cross-range position Δc_P of a point P obtained from an interferometric pair (see Fig. 7) can be given by [25, pp. 113–130]

$$\begin{aligned}\Delta c_P &= -c_P^0 \cdot \frac{|\mathcal{E}|\cos(\theta-\beta)}{B_\perp^0} \\ &= -c_P^0 \cdot \frac{\mathcal{E}_\perp}{B_\perp^0} \end{aligned} \tag{9}$$

where c_P^0 is the initial cross-range position computed with perpendicular baseline $B_\perp^0$, ignoring the residual perpendicular baseline $\mathcal{E}_\perp$ caused by the orbit error $\mathcal{E}$. θ is the look angle. Assuming a Gaussian distributed perpendicular baseline error with a standard deviation $\sigma_{\mathcal{E}_\perp}$, the uncertainty in cross-range $\sigma_{c_{P,\text{orb}}}$ can be written by

$$\sigma_{c_{P,\text{orb}}} = \frac{c_P^0}{B_\perp^0} \cdot \sigma_{\mathcal{E}_\perp}. \tag{10}$$

The larger the perpendicular baseline, the lower the impact of the state vector errors on the cross-range computation.

Nonparallel orbits might cause decorrelation (a small reduction in SCR due to viewing angle differences) and a phase ramp in azimuth direction in the interferograms. The decorrelation can be neglected for our case since we work with PSs (pointlike targets). In our PSI stack processing, a phase deramping operation is performed to remove the phase trend.

2) Impact of the SCR of Scatterers: Given the SCR of a target (P), the impact of interferometic phase variance σ_{ϕ_P} on the precision of cross-range $\sigma_{c_{P,\text{SCR}}}$ can be approximated (for SCR $>$ 1 dB) by [25, pp. 34–50] [26]

$$\begin{aligned}\sigma_{c_{P,\text{SCR}}} &= \frac{\lambda\, r_P}{4\pi\, B_\perp} \cdot \sigma_{\phi_P} \\ &\approx \frac{\lambda\, r_P}{4\pi\, B_\perp} \cdot \sqrt{\frac{2}{2\ \text{SCR} - 0.55}} \end{aligned} \tag{11}$$

where λ is the radar wavelength.

3) Phase Center of the Reference Point: The position of a reference point R plays a role during the geocoding when radar coordinates are transformed to terrestrial reference frame (TRF) coordinates. The bias and precision in the cross-range position of the reference point R impacts the 3-D position and precision of the rest of the scatterers. The impact of a cross-range error is listed in the terms $((\partial e/\partial c), (\partial n/\partial c), (\partial h/\partial c))$ in Table I (column $\kappa = c$) and Fig. 2.

The cross-range bias of the reference point R can be mitigated in two ways. First, a mean ground height of the area (we assume that most of the PSs are from the ground level) is obtained from the mode of the histogram of PS heights (which is relative to a reference point). Similarly, a mode computed from the histogram of heights from a high-precision digital elevation model gives an alternate estimate of the same ground level. A difference in these two mode values provides the height of the reference point R above the reference surface [27]. The second approach is to measure *in situ* the phase center of a reference scatterer. A convenient approach would be to use a known geometric structure with well-defined phase center, such as a CR or TR, as a reference point [11], [28], [29]. The uncertainty in the cross-range position of reference point ($\sigma_{c_R}^2$) can be given by

$$\sigma_{c_R} = \frac{\sigma_{H_R}}{\sin(\theta_{\text{inc},R})} \tag{12}$$

where σ_{H_R} is the precision of reference point height H_R above a reference surface (see Fig. 4) and $\theta_{\text{inc},R}$ is the incidence angle at the location of the reference point R.

C. Geocoding and Datum Transformation From Radar to Local Coordinates

Geocoding is applied on the corrected (r_P, a_P, c_P) coordinates [from (1) and (7)] to transform to TRF coordinates [15], [16]. The datum transformation between TRF coordinates and the local (Dutch) coordinates (e_P, n_P, h_P) (expressed in north, east, and height) was performed using the RDNAPTRANS procedure [30]. This procedure employs a geoid model for the vertical component. The position error (assumed diagonal) variance–covariance (VC) matrix Q_{rac} in radar coordinates is given by

$$Q_{\text{rac}} = \begin{bmatrix} \sigma_{r_P}^2 & & \\ & \sigma_{a_P}^2 & \\ & & \sigma_{c_P}^2 \end{bmatrix}. \tag{13}$$

Then, using an S-transformation (described in [12]), the 3-D position VC matrix in radar Q_{rac} is propagated to the VC matrix in local coordinates Q

$$\underline{\widehat{P}} \sim \mathcal{N}(\mu,\ Q)$$

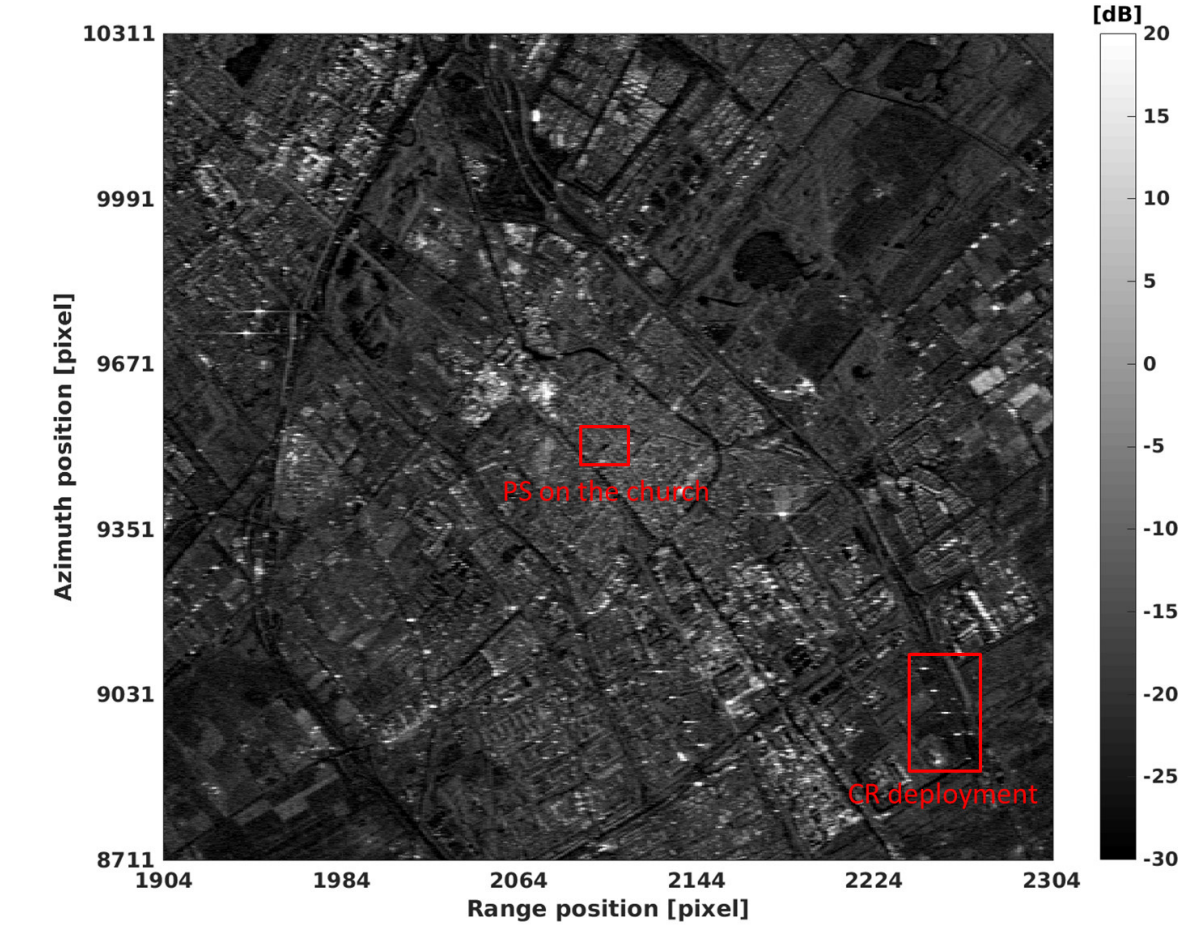

Fig. 8. Mean backscatter image (averaged 44 ASAR images and expressed in dB) covering Delft. (a) CR deployment and the infrastructure of interest regions highlighted in red box. (b) Mean backscattering response of CRs deployed at a test site (for optical image, see Fig. 9). (c) Location of the six PSs detected on the infrastructure of interest shown in Fig. 15. The results of PSs linked to targets are demonstrated in Fig. 16.

with

$$\mu = \begin{bmatrix} e_P \\ n_P \\ h_P \end{bmatrix} \text{ and } Q = \begin{bmatrix} \sigma_e^2 & \sigma_{en}^2 & \sigma_{eh}^2 \\ \sigma_{en}^2 & \sigma_n^2 & \sigma_{nh}^2 \\ \sigma_{eh}^2 & \sigma_{nh}^2 & \sigma_h^2 \end{bmatrix} \tag{14}$$

where μ and Q are the estimated 3-D position in local coordinates and its VC matrix, respectively. The diagonal (σ_e^2, σ_n^2, and σ_h^2) and nondiagonal (σ_{en}^2, σ_{eh}^2, and σ_{nh}^2) entries are the variances and covariances in east, north, and height coordinates, respectively.

D. Linking Radar Scatterers to Objects

Scatterer-to-object linking is a step to associate a scatterer with a 3-D position and a VC matrix to a position on a

real-world object or a point from a set of K potential points from, e.g., a scan of the environment. This step is facilitated by using point cloud data from the objects, with its quality expressed by a 3×3 VC matrix for each point along with its position. A radar scatterer can be linked to the nearest point, in the metric defined by both VC matrices. The VC matrix not only represents the radar acquisition geometry but is also very helpful in constraining the 3-D search space to link a scatterer to a point from a point set.

To perform this linking, we exploit a similarity (closeness) measure ($\mathbb{B}$) between a radar scatterer position $\underline{P}$ and the position $\underline{P}_i$ of the ith point of a 3-D object model, e.g., a building facade, building roof, bridge, or pole. Similarity between two populations with associated probability density functions (pdfs) is given by [31]–[33], [34, pp. 20–65]

$$\int \sqrt{\text{pdf}(\underline{P})}\ \sqrt{\text{pdf}(\underline{P}_i)}\ df \tag{15}$$

where f is the 3-D space defined by $(e,\ n,\ h)$. The positions $\underline{P} \sim \mathcal{N}(\mu,\ Q)$ and $\underline{P}_i \sim \mathcal{N}(\mu_i,\ Q_i)$ are trivariate Gaussian distributed. For the case of Gaussian pdfs, the above-mentioned integral can be evaluated by an exponential function [34, pp. 20–65]

$$e^{g(\omega)} \quad \text{with } \omega = 0.5 \tag{16}$$

and

$$g(\omega) = \frac{\omega\ (1-\omega)}{2}(\mu_i - \mu)^T[\omega\ Q + (1-\omega)\ Q_i]^{-1}(\mu_i - \mu) + \frac{1}{2}\log\left(\frac{|\omega\ Q + (1-\omega)\ Q_i|}{|Q|^{\omega}\ |Q_i|^{1-\omega}}\right) \tag{17}$$

where $|.|$ is the determinant of a matrix. Then, the Bhattacharyya measure $\mathbb{B}_i$ between $\underline{P}$ and $\underline{P}_i$ can be written as [32], [35]

$$\mathbb{B}_i\left(\underline{P}, \underline{P}_i\right) = \frac{1}{8}\left[(\mu_i - \mu)^T\left(\frac{Q+Q_i}{2}\right)^{-1}(\mu_i - \mu)\right] + \frac{1}{2}\left[\log\left|\left(\frac{Q+Q_i}{2}\right)\right| - \frac{1}{2}\log|Q| - \frac{1}{2}\log|Q_i|\right] \quad \text{for } i = 1, \ldots, K. \tag{18}$$

The measure $\mathbb{B}_i$ compares two distributions rather than just their means. In this aspect, the similarity measure is preferred over the weighted squared norm $\|\underline{P} - \underline{P}_i\|_{Q+Q_i}$ (chi-squared test statistic) [36], [37].

The radar scatterer with position $\underline{P}$ is then associated with an object i located at $\underline{P}_{i,T}$ with the minimum Bhattacharyya measure

$$\min_{\text{find } i\ \in\ (1,K)} \left\{\mathbb{B}_i(\underline{P}, \underline{P}_i)\right\} \tag{19}$$

where K is the number of possible real-world points in the vicinity of a radar scatterer.

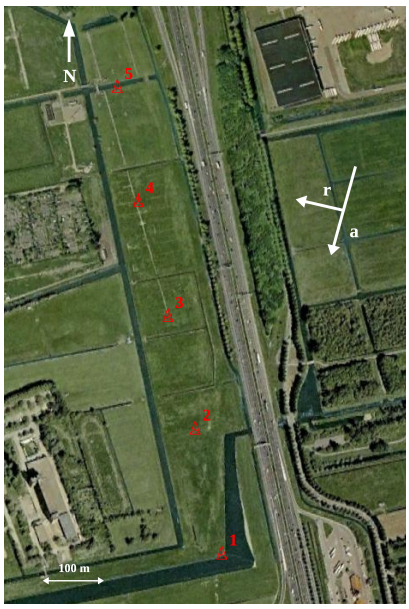

Fig. 9. Delft CR experiment setup for ENVISAT ASAR descending acquisitions. CR and their numbers are marked in red as shown in the GoogleEarth (optical image date: May 19, 2004) [21].

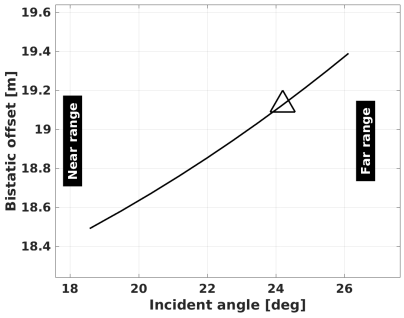

Fig. 10. Azimuth bistatic offset computed along the swath of an ENVISAT ASAR descending acquisition (February 21, 2007). The magnitude of bistatic offset at the location of the CR5 is marked with a triangle.

III. Experiment Setup and Results

We investigated the positioning performance of medium-resolution SLC images covering Delft, The Netherlands. The mean intensity image from ASAR over Delft is shown in Fig. 8. The procedure described in Section II was tested with CRs from a field experiment [see Fig. 8(b)] and "natural" coherent scatterers from PSI [see Fig. 8(c)]. In both cases, the scatterer positions estimated from SAR were compared with the ground-truth position. The ground-truth position, the phase center of a scatterer, was obtained with the aid of differential global positioning system (DGPS) for the CRs and LiDAR for validating natural coherent scatterers.

A. Setup

Five trihedral CRs (1.43 m sides) oriented (see Fig. 9) toward ENVISAT ASAR IMS descending acquisitions from November 2003 to June 2008 were used. CR1 and CR2 were later destroyed and stolen, respectively, and did not serve the whole experiment period, and therefore, CR3, CR4,

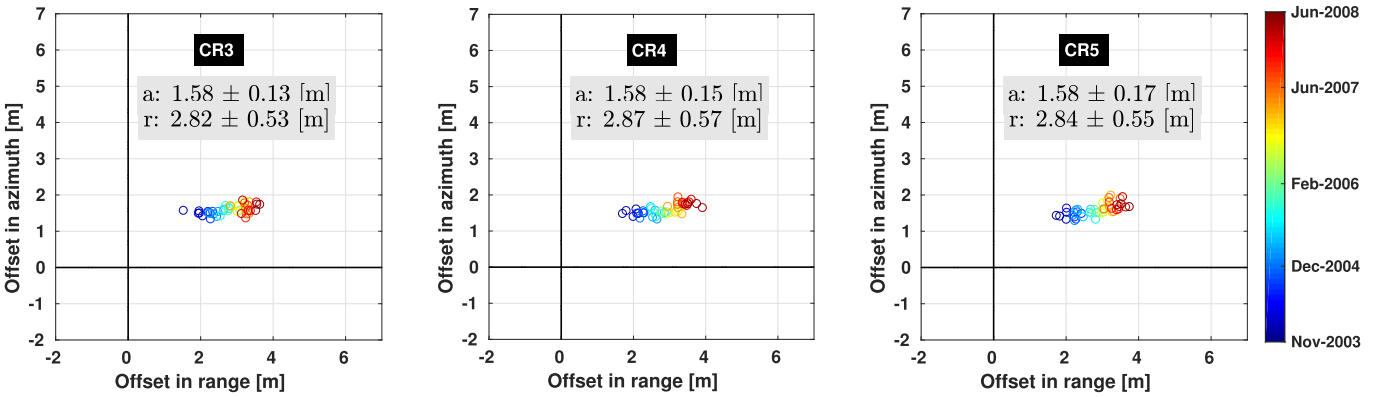

Fig. 11. 2-D position offsets of CR with azimuth bistatic (as shown in Fig. 10), SET, atmosphere (with respect to mean), and plate tectonics corrections. The position errors are reported with respect to the desired offset of (0, 0), highlighted with bold lines. The estimated azimuth and range one-time calibration offsets are: $\widehat{a}_{\text{cal}} = 1.58$ m and $\widehat{r}_{\text{cal}} = 2.84$ m.

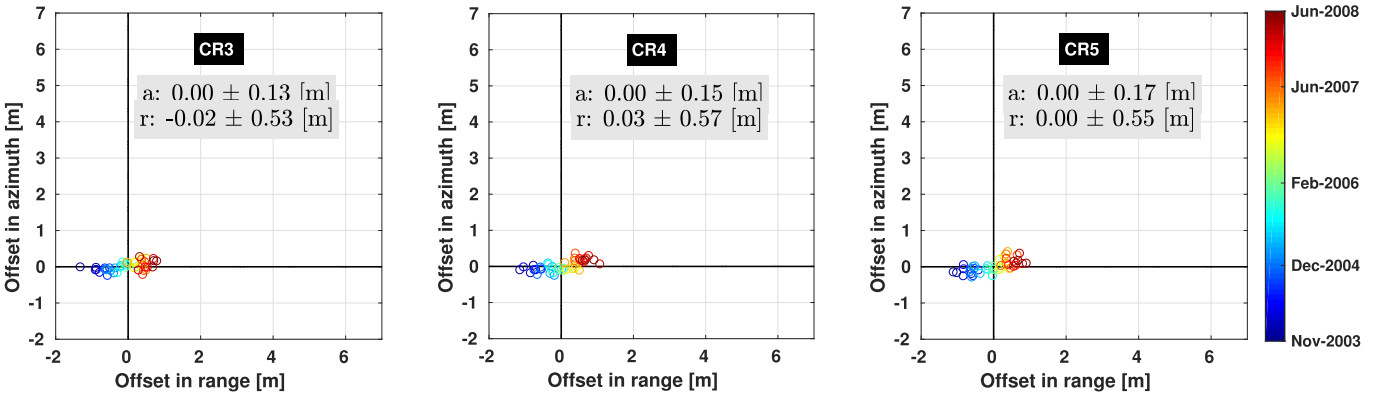

Fig. 12. 2-D position offsets of CR with the bistatic, SET, atmospheric path delay, plate motion, and calibration offset corrections. The azimuth (a) and range (r) offsets and the resulting precisions are indicated in the plot for each CR.

and CR5 were used in this paper. The CRs were oriented for 44 IMS mode IS2 swath acquisitions with an incidence angle of 24.2° and a heading angle of 196.2°. The IMS SLC images have a pixel spacing of approximately 4 and 8 m in azimuth and (slant) range, respectively. They were acquired in VV polarization and came with a geometric resolution of ∼9 m in slant range and 6 m in azimuth. Here, the image pixels were oversampled by a factor of 128 × 128, using an FFT, to detect the subpixel positions. The chosen oversampling factor introduced a quantization error of approximately 1 cm in azimuth and 2 cm in range in determining the pixel peak. For validation, the CR ground-truth positions were measured with DGPS real time kinematic in European Terrestrial Reference Frame 1989 (ETRF89), provided with a 1–2 cm 3-D precision.

B. Empirical Computation of 2-D Residual Calibration Offsets

The error sources in azimuth and range (see Section II) were mitigated step by step; the results are shown in Figs. 11–13. The impact of the bistatic effect in the ASAR IMS imagery is shown in Fig. 10. The bistatic azimuth shift at the location of the CR (around 19 m) has been computed and removed in Fig. 11. In addition, the plate motion corrections were performed in order to compare the ground-truth CR measurements (given in ETRF89) with ASAR data (with orbits provided in International Terrestrial Reference Frame). The residual position errors were dominated by the existence of unmodeled calibration offsets [see Section II-A3 and (1)]. These azimuth and range residual calibration offsets were estimated to be $\hat{a}_{\text{cal}} = 1.58$ m and $\hat{r}_{\text{cal}} = 2.84$ m, respectively. The SLC images used in this paper already included the December 13, 2003 SWST bias updates. Therefore, as explained in Section II-A2, the variability with respect to their mean path delay and SET was mitigated. After application of calibration offsets in Fig. 12, it can be clearly seen that the position is drifting in range as discussed in Section II-A1. Finally, the corrections due to LO drift from (2) were incorporated in pulse repetition frequency and SWST; the results are presented in Fig. 13. LO drift compensation provided a significant improvement of about 460% (CR5) in the range positioning and a minor 1% improvement in azimuth. The above-mentioned corrections result in improved 2-D positioning and led to an accuracy of 11 cm in azimuth (CR3) and 12 cm in range (CR5) (see Fig. 13). Compared with earlier studies, which reached a position accuracy in the order of meters (see [38]–[40]), the achieved accuracy is an order of magnitude better. Similar improvements were demonstrated for the case of Sentinel-1A/1B [41].

C. 3-D Position Accuracy for Reflectors

For the cross-range position, PSI was applied on a set of 44 ASAR IMS (swath IS2) descending mode acquisitions

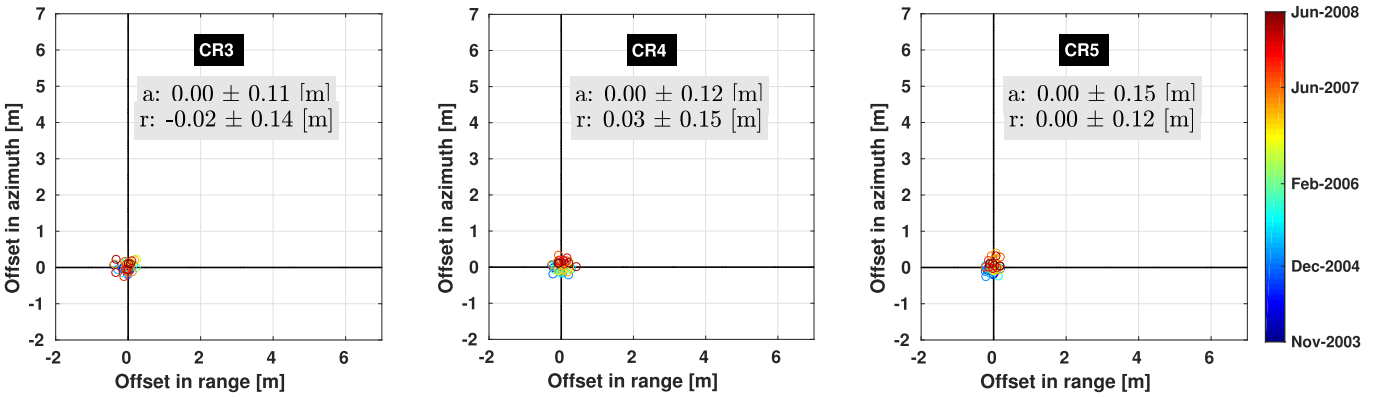

Fig. 13. Unbiased 2-D positioning capability of ENVISAT ASAR products. The overall corrections applied were the bistatic, SET, path delay (ionosphere and troposphere), plate motion, calibration offsets, and LO drift.

TABLE II
SCR AND AMPLITUDE DISPERSION (D_A) VALUES EXHIBITED BY THE PSs DETECTED OVER THE CHURCH

PS #	SCR (dB)	D_A
1	18.9	0.43
2	17.1	0.26
3	14.0	0.32
4	16.4	0.25
5	14.7	0.24
6	13.1	0.37

covering Delft. The image acquired on February 21, 2007 was used as a master image. The position corrections in azimuth and range, as mentioned in Section III-B, were performed with respect to the master image pixels. The LO drift corrections from (2) were applied to the master image timing parameters. CR3 was used as reference R (see Fig. 4). Fixing the phase center of reference point R to the apex of CR3 with centimeter accuracy eliminates the cross-range bias in the 3-D position estimation. The position of the other two CR was transformed into (e, n, h) coordinates, (see Section II-C), and the positioning VC matrix was propagated from radar (Q_{rac}) to local (Q_{enh}) coordinates [12].

The CRs used in this paper had an average SCR of about 35 dB and exhibited a normalized amplitude dispersion of ∼0.05. If we consider an orbit precision of $\sigma_{\mathcal{E}_\perp} = 10$–$20$ cm and an average perpendicular baseline of the stack of about 450 m (as observed in our time series), a cross-range precision of $\sigma_{c_{P,\text{orb}}} = 3$–$5$ cm was noticed for a target of 50 m height. We used a CR with a known position as reference, and σ_{c_R} of ∼2 cm was observed. In our InSAR stack processing, the impact of $\sigma_{c_{P,\text{SCR}}}$ was found to be a dominant factor in σ_{c_P} [see (8) and (11)]. The application of position corrections resulted in the 3-D position accuracy of 0.28 m (CR4) and 0.53 m (CR5) with the quality of 3-D position expressed as an error ellipsoid with a ratio of axis lengths $(1/(\sigma_{a_P}/\sigma_{r_P})/(\sigma_{c_P}/\sigma_{r_P}))$ 1/0.8/12 (with $\sigma_r = 15$ cm) (CR4) and 1/1/15 (with $\sigma_r = 12$ cm) (CR5), respectively. The results of CR4 and CR5 are in the same order of magnitude; therefore, we plot only the results of CR4 in Fig. 14. The estimated

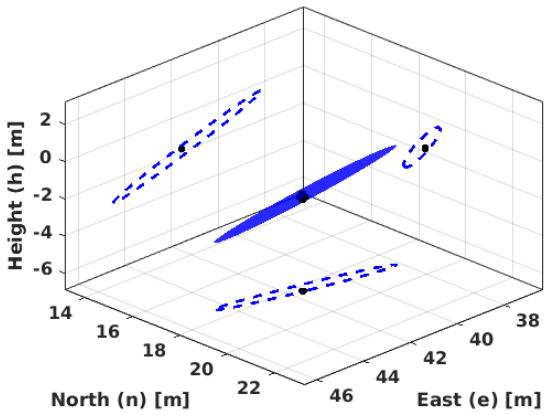

Fig. 14. 3-D accuracy of CR4 was 0.28 m with its 3-D uncertainty drawn using error ellipsoid (1σ confidence interval) relative to the ground truth indicated by the black dot. It exhibited an elongated (prolate) error ellipsoid with a ratio of axis lengths 1/0.8/12 (with $\sigma_r = 0.15$ m). The ratio of axis lengths represents the precision in range, azimuth, and cross range relative to range, respectively. The error ellipsoid is projected in *en*, *nh*, and *he* planes (indicated with dashed lines) to illustrate their intersection with the ground-truth position (black dot).

Fig. 15. Infrastructure of interest (a church) in Delft region shown in GoogleEarth (optical image date: May 19, 2004) [21].

position of CR4 (in blue) is drawn in comparison with its ground-truth position (in black) along with its respective error ellipsoid. The position error ellipsoids for ASAR are elongated in the cross-range direction, resembling a cigar-shaped ellipsoid. The intersection of the scaled error ellipsoid (in blue)

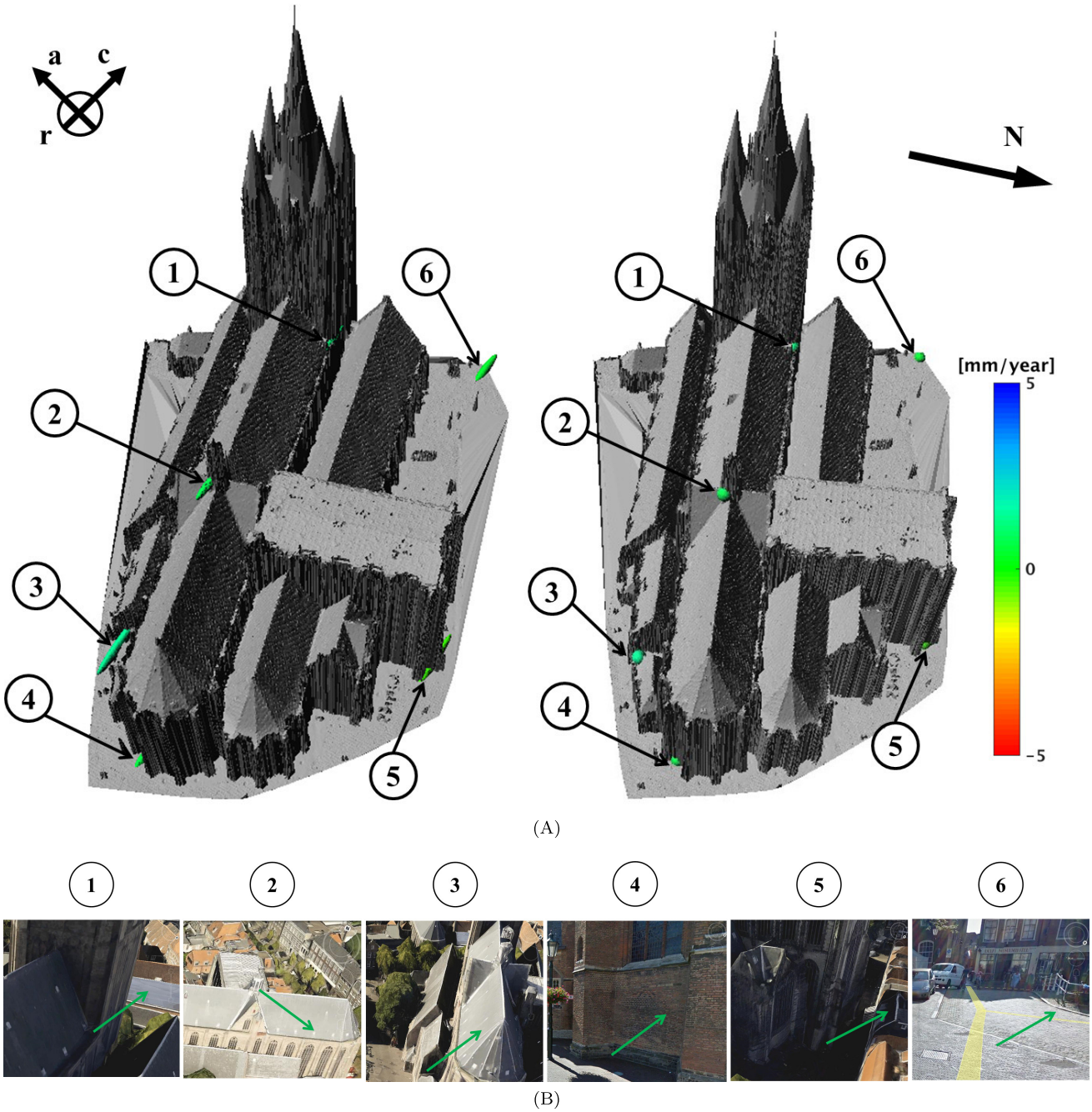

Fig. 16. Results of linking radar scatterers from ENVISAT ASAR to a church in Delft using the 3-D city model (in gray). Here, the opportunistic coherent scatterers of the church are presented. (a) (Left) Scatterers with position error ellipsoids (2σ confidence level). (Right) Results of scatterers after linking to objects on the church as a dot (size scaled just to ease visualization). The color coding of ellipsoids and dots is based on their deformation rate in mm/year. (b) Optical image showing each of the linked objects. It is hypothesized that the scatterers ①, ④, and ⑤ are trihedral reflectors, while object ⑥ is a single-bounce reflector. Objects ② and ③ are either single-bounce or multibounce reflectors. Here, the scatterers ①–③ are from the church, ④ and ⑤ are from church and ground interaction, and ⑥ is from the ground. Interpretation: the reflections from the church (①–⑤) and the ground (⑥) were found to exhibit no significant linear deformation (see Fig. 17).

with the ground-truth position (in black) shows that the geolocalization corrections were successful.

D. Linking Coherent Scatterers to Objects

In this section, we present the 3-D positioning results of opportunistic coherent scatterers from ENVISAT ASAR IMS acquisitions covering Delft. A normalized amplitude dispersion threshold of 0.5 was used to detect PS (opportunistic coherent scatterers) in our PSI processing [5]. The scatterers from the church [see Figs. 8(c) and 15] were detected as PSs. They exhibited an average SCR of about 13–19 dB and an amplitude dispersion of 0.2–0.4 (see Table II).

The error correction, PSI processing, and the position ellipsoid per scatterer was computed as in Section III-C for a church (see Fig. 15). The coherent scatterers with their

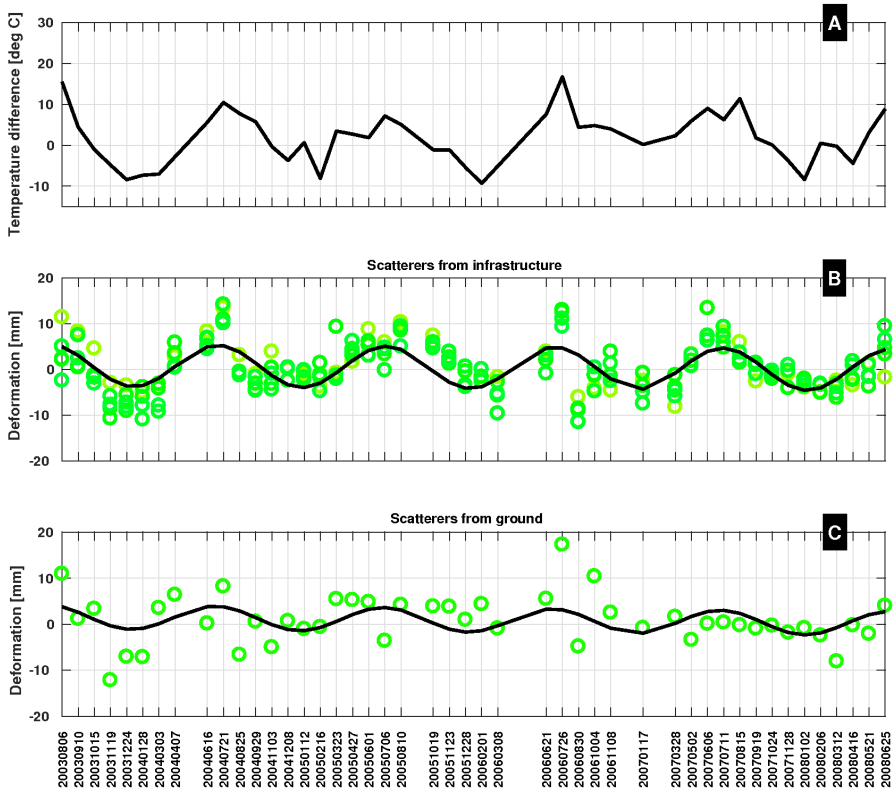

Fig. 17. Interpreting the deformation of scatterers after linking to objects in Fig. 16. LOS deformations in (B) and (C) are drawn with color circles. Their colors are based on their linear deformation rate identical to Fig. 16. In (A), the black line shows 24-h average temperature from a meteorological station at the time of satellite acquisition with respect to the master image. (B) and (C) Kinematic time series of scatterers linked to the infrastructure and the ground, respectively. The black line in (B) and (C) represents a seasonal deformation model for the scatterers from the infrastructure (①–⑤ in Fig. 16) and the ground (⑥ in Fig. 16), respectively. Here, the seasonal signal (due to temperature) from the infrastructure [black line in (B)] was stronger than the ground [black line in (C)].

VC matrix drawn as error ellipsoids (2σ confidence level) are shown with a 3-D model in Fig. 16(a) (left). A 3-D city model was constructed using the high-quality LiDAR data as described in [42]. The quality of LiDAR point positions is considered to have a VC matrix $Q_i = \sigma^2 I$ [see (18)] with $\sigma = 0.1$ m, and I is a 3×3 identity matrix [43], [44]. Then, using (18), the radar scatterers were linked (associated) with the positions on the church (see Fig. 16(a) (right)]. The scatterer's error ellipsoid [see Fig. 16(a) (left)] and the intersection point on the church [see Fig. 16(a) (right)] are colored based on their deformation rate. For validation, the associated scatterers were individually visualized with optical images [see Fig. 16(b)]. From these visualizations, it is considered that the scatterers ①, ④, and ⑤ were trihedral CRs, while object ⑥ is a single-bounce reflector. Objects ②, and ③ are either single-bounce or multibounce reflectors. Here, the scatterers ①–③ were from the church, ④ and ⑤ were from church and ground interaction, and ⑥ from the ground. Even after applying position error corrections, some of the scatterer phase centers were found inside the buildings and below the ground level [see ①, ⑤, and ⑥ in Fig. 16(a) (left)]. Similar scenarios were also observed by [9] and [45]. We believe this behavior is due to the influence of signal contributions from the scatterers in the (urban) neighborhood. In spite of this, we were able to associate scatterers with their geometrically most probable position in the 3-D model as shown in Fig. 16(a) (right), based on the exploitation of the position error ellipsoids and the availability of the LiDAR data. For the case when the phase center (in the case of multiple reflections) is not present in the 3-D model, our approach will associate the scatterer with an object (in the 3-D model) depending on the position error ellipsoid's orientation and proximity. From this linking, it was evident that the main tower of this church was not measured by PS from the ASAR track and the scatterers from the other parts of the church showed seasonal deformation patterns [see Fig. 17(A) and (B)], while the reflections from the ground showed a weak seasonal pattern as shown in Fig. 17(C). The deformation pattern of the ground and the infrastructure is attributed to temperature and ground water level variability [46]. Fig. 17(A) shows the one-day average temperature during each ASAR acquisition relative to the master acquisition. The meteorological data were obtained from a weather station located approximately 8 km from this location.

By associating the scatterer's phase center with objects, each scatterer's estimated deformation can be interpreted to a depth necessary for a certain application. Such linking could improve our understanding and pave the way for applications, such as infrastructure-specific monitoring and stability analysis, relative stress on underground infrastructure [47], [48], and designing construction of new infrastructure (cities, buildings, dikes, and so on) to enhance InSAR measurement sampling.

IV. Conclusion

We applied a systematic procedure to precisely estimate the radar scatterer position and the subsequent quality description for medium-resolution SAR imagery and demonstrated a method for radar scatterer to object linking. The method was assessed using five years of ASAR imagery for a test site in Delft using DGPS and LiDAR.

As mean atmospheric and geodynamic corrections were implicitly incorporated in the 2003 SWST bias update, these corrections are not necessary. Therefore, only epoch-dependent atmosphere and SET corrections with respect to their mean value were applied here. Furthermore, the application of plate motion and bistatic corrections helped us in identifying the existence of residual calibration offsets. These residual calibration offsets, considered as a refinement to the December 12, 2003 SWST bias update, were empirically computed to be about 1.58 m in azimuth and 2.84 m in range. The application of LO drift corrections showed significant improvements from 55 to 12 cm (CR5) in the range precision. This proposed procedure (consisting of bistatic, path delay, SET, LO, and calibration corrections) is "tie-point free" and can be applied to all ASAR products in order to deliver a more accurate 2-D positioning capability. From our CR experiment site, we showed that we were able to accomplish an accuracy of up to 11 cm (CR3) and 12 cm (CR5) in azimuth and range, respectively. These improvements should serve as a reference for other medium-resolution sensors, such as ERS-1/2, RadarSAT-2, and Sentinel-1A/B.

In 3-D, the trihedral CR's position and error ellipsoid were validated using DGPS measurements, and an absolute positioning of about 0.28 m for CR4 and 0.53 m for CR5 was achieved. The error ellipsoids were cigar-shaped; their intersection with GPS positions justified the method of linking the scatterer's phase center to objects. The method was also applied to other non-CR coherent scatterers, and using their error ellipsoids, scatterers were associated with objects (points) in the 3-D city model. The results of linking and interpretation were demonstrated over a building in Delft (see Figs. 16 and 17). In spite of using medium-resolution ASAR IMS imagery, the results established the capability of monitoring (parts of) individual infrastructure.

Acknowledgment

The authors would like to thank G. Ketelaar, P. Marinkovic, and others from the Delft University of Technology for contributing to the Delft ENVISAT ASAR CR experiment. They would like to thank J. Lesparre for informative discussions in constructing the 3-D city model. They would also like to thank the European Space Agency for providing the ENVISAT ASAR time-series images over Delft. They are grateful to the anonymous reviewers for their constructive comments.

References

[1] S. Usai and R. F. Hanssen, "Long time scale INSAR by means of high coherence features," in *Proc. 3rd ERS Symp.-Space Service Environ.*, Florence, Italy, Mar. 1997, pp. 225–228.

[2] S. Usai and R. Klees, "SAR interferometry on very long time scale: A study of the interferometric characteristics of man-made features," *IEEE Trans. Geosci. Remote Sens.*, vol. 37, no. 4, pp. 2118–2123, Jul. 1999.

[3] A. Ferretti, C. Prati, and F. Rocca, "Permanent scatterers in SAR interferometry," in *Proc. Int. Geosci. Remote Sens. Symp.*, Hamburg, Germany, Jun./Jul. 1999, pp. 1528–1530.

[4] A. Ferretti, C. Prati, and F. Rocca, "Permanent scatterers in SAR interferometry," *IEEE Trans. Geosci. Remote Sens.*, vol. 39, no. 1, pp. 8–20, Jan. 2001.

[5] B. M. Kampes, "Displacement parameter estimation using permanent scatterer interferometry," Ph.D. dissertation, Fac. Civil Eng. Geosci., Delft Univ. Technology, Delft, The Netherlands, Sep. 2005.

[6] M. Eineder, C. Minet, P. Steigenberger, X. Cong, and T. Fritz, "Imaging geodesy—Toward centimeter-level ranging accuracy with TerraSAR-X," *IEEE Trans. Geosci. Remote Sens.*, vol. 49, no. 2, pp. 661–671, Feb. 2011.

[7] A. Schubert, M. Jehle, D. Small, and E. Meier, "Influence of atmospheric path delay on the absolute geolocation accuracy of TerraSAR-X high-resolution products," *IEEE Trans. Geosci. Remote Sens.*, vol. 48, no. 2, pp. 751–758, Feb. 2010.

[8] S. Auer, S. Hinz, and R. Bamler, "Ray-tracing simulation techniques for understanding high-resolution SAR images," *IEEE Trans. Geosci. Remote Sens.*, vol. 48, no. 3, pp. 1445–1456, Mar. 2010.

[9] A. Schunert and U. Soergel, "Assignment of persistent scatterers to buildings," *IEEE Trans. Geosci. Remote Sens.*, vol. 54, no. 6, pp. 3116–3127, Jun. 2016.

[10] P. Dheenathayalan, A. Schubert, D. Small, and R. F. Hanssen, "3D geolocation error of radar pixels: Modeling, propagation and mitigation," in *Proc. Eur. Space Agency Living Planet Symp.*, Edinburgh, U.K., Sep. 2013, pp. 9–13.

[11] P. Dheenathayalan, D. Small, and R. F. Hanssen, "3D geolocation capability of medium resolution SAR sensors," in *Proc. Int. Geosci. Remote Sens. Symp. (IGARSS), 35th Can. Symp. Remote Sens. (CSRS)*, Québec, QC, Canada, Jul. 2014, pp. 13–18.

[12] P. Dheenathayalan, D. Small, A. Schubert, and R. F. Hanssen, "High-precision positioning of radar scatterers," *J. Geodesy*, vol. 90, no. 5, pp. 403–422, 2016.

[13] X. X. Zhu, S. Montazeri, C. Gisinger, R. F. Hanssen, and R. Bamler, "Geodetic SAR tomography," *IEEE Trans. Geosci. Remote Sens.*, vol. 54, no. 1, pp. 18–35, Jan. 2016.

[14] C. Gisinger *et al.*, "Precise three-dimensional stereo localization of corner reflectors and persistent scatterers with TerraSAR-X," *IEEE Trans. Geosci. Remote Sens.*, vol. 53, no. 4, pp. 1782–1802, Apr. 2015.

[15] G. Schreier, *SAR Geocoding: Data and Systems*. Karlsruhe, Germany: Wichmann Verlag, 1993.

[16] D. Small, P. Pasquali, and S. Füglistaler, "A comparison of phase to height conversion methods for SAR interferometry," in *Proc. Int. Geosci. Remote Sens. Symp.*, Lincoln, NE, USA, vol. 1, May 1996, pp. 342–344.

[17] D. Small, B. Rosich-Tell, A. Schubert, E. Meier, and D. Nüesch, "Geometric validation of low and high-resolution ASAR imagery," in *Proc. ENVISAT ERS Symp.*, Salzburg, Austria, Sep. 2004, p. 9.

[18] P. Marinkovic and Y. Larsen, "Consequences of the local oscillator drift model for ENVSAT ASAR—Significant improvement of the localization accuracy," in *Proc. CEOS Calibration Validation Workshop*, Noordwijk, The Netherlands, Oct. 2015, pp. 1–32.

[19] R. F. Hanssen, T. M. Weckwerth, H. A. Zebker, and R. Klees, "High-resolution water vapor mapping from interferometric radar measurements," *Science*, vol. 283, no. 5406, pp. 1297–1299, 1999. [Online]. Available: http://science.sciencemag.org/content/283/5406/1297

[20] B. R. Bean and E. J. Dutton, *Radio Meteorology*. New York, NY, USA: Dover, 1968.

[21] GoogleInc. (2017). *Google Earth (Version 7.1.5.1557)*. [Online]. Available: http://www.earth.google.com

[22] T. Fritz, "TerraSAR-X ground segment level 1b product format specification," DLR, Oberpfaffenhofen, Germany, Tech. Rep. TX-GS-DD-3307, 2007.

[23] D. Small, B. Rosich-Tell, E. Meier, and D. Nüesch, "Geometric calibration and validation of ASAR imagery," in *Proc. CEOS WGCV SAR Calibration Validation Workshop*, Ulm, Germany, May 2004, p. 8.

[24] E. Meier, U. Frei, and D. Nüesch, *Precise Terrain Corrected Geocoded Images*, G. Schreier, Ed. Karlsruhe, Germany: Verlag GmbH, 1993, ch. 7, pp. 173–185.

[25] R. F. Hanssen, *Radar Interferometry: Data Interpretation and Error Analysis*. Dordrecht, The Netherlands: Kluwer, 2001.

[26] P. Dheenathayalan, M. C. Cuenca, P. Hoogeboom, and R. F. Hanssen, "Small reflectors for ground motion monitoring with InSAR," *IEEE Trans. Geosci. Remote Sens.*, vol. 55, no. 12, pp. 6703–6712, Dec. 2017.
[27] P. Dheenathayalan and R. F. Hanssen, "Radar target type classification and validation," in *Proc. IEEE Int. Geosci. Remote Sens. Symp.*, Melbourne, VIC, Australia, Jul. 2013, pp. 923–926.
[28] A. Ferretti *et al.*, "Submillimeter accuracy of InSAR time series: Experimental validation," *IEEE Trans. Geosci. Remote Sens.*, vol. 45, no. 5, pp. 1142–1153, May 2007.
[29] P. S. Mahapatra, S. Samiei-Esfahany, H. van der Marel, and R. F. Hanssen, "On the use of transponders as coherent radar targets for SAR interferometry," *IEEE Trans. Geosci. Remote Sens.*, vol. 52, no. 3, pp. 1869–1878, Mar. 2014.
[30] A. de Bruijne, J. van Buren, A. Kösters, and H. van der Marel, "Geodetic reference frames in the Netherlands," Definition Specification ETRS89, RD, NAP, Their Mutual Relationships, Delft, the Netherlands Geodetic Commission, Tech. Rep., 2005.
[31] P. C. Mahalanobis, "On the generalized distance in statistics," in *Proc. Nat. Inst. Sci. India*, vol. 2, no. 1, pp. 49–55, 1936.
[32] A. Bhattacharyya, "On a measure of divergence between two multinomial populations," *Sankhyā*, vol. 7, no. 4, pp. 401–406, 1946.
[33] K. Matusita, "Decision rules, based on the distance, for problems of fit, two samples, and estimation," *Ann. Math. Statist.*, vol. 26, no. 4, pp. 631–640, 1955.
[34] R. Duda, P. Hart, and D. Stork, *Pattern Classification*. Hoboken, NJ, USA: Wiley, 2012.
[35] T. Kailath, "The divergence and Bhattacharyya distance measures in signal selection," *IEEE Trans. Commun. Technol.*, vol. TCOM-15, no. 1, pp. 52–60, Feb. 1967.
[36] P. J. G. Teunissen, *Testing Theory; An Introduction*, 1st ed. Delft, The Netherlands: Delft Univ. Press, 2000.
[37] F. J. Aherne, N. A. Thacker, and P. I. Rockett, "The Bhattacharyya metric as an absolute similarity measure for frequency coded data," *Kybernetika*, vol. 34, no. 4, pp. 363–368, 1998.
[38] D. Small, A. Schubert, B. Rosich, and E. Meier, "Geometric and radiometric correction of ESA SAR products," in *Proc. ESA ENVISAT Symp.*, Montreux, Switzerland, Apr. 2007, p. 6.
[39] N. Miranda *et al.*, "The ENVISAT ASAR mission: A look back at 10 years of operation," in *Proc. ESA*, vol. 722, 2013, p. 41.
[40] A. Schubert, D. Small, M. Jehle, and E. Meier, "COSMO-Skymed, TerraSAR-X, and RADARSAT-2 geolocation accuracy after compensation for earth-system effects," in *Proc. IEEE Int. Geosci. Remote Sens. Symp.*, Jul. 2012, pp. 3301–3304.
[41] A. Schubert, N. Miranda, D. Geudtner, and D. Small, "Sentinel-1A/B combined product geolocation accuracy," *Remote Sens.*, vol. 9, no. 6, p. 607, 2017. [Online]. Available: http://www.mdpi.com/2072-4292/9/6/607
[42] J. Lesparre and B. Gorte, "Simplified 3D city models from LiDAR," in *Proc. ISPRS-Int. Arch. Photogramm., Remote Sens. Spatial Inf. Sci.*, vol. 1, 2012, pp. 1–4.
[43] N. V. der Zon, "Kwaliteitsdocument AHN-2," (in Dutch), Rijkswaterstaat, Waterschappen, The Netherlands, Tech. Rep. version 1.3, 2011, vol. 1, p. 1. [Online]. Available: http://www.ahn.nl/binaries/content/assets/hwh—ahn/common/wat+is+het+ahn/kwaliteitsdocument_ahn_versie_1_3.pdf
[44] C. van der Sande, S. Soudarissanane, and K. Khoshelham, "Assessment of relative accuracy of ahn-2 laser scanning data using planar features," *Sensors*, vol. 10, no. 9, pp. 8198–8214, 2010.
[45] S. Auer, S. Gernhardt, and R. Bamler, "Ghost persistent scatterers related to multiple signal reflections," *IEEE Geosci. Remote Sens. Lett.*, vol. 8, no. 5, pp. 919–923, Sep. 2011.
[46] F. van Leijen and R. F. Hanssen, "Ground water management and its consequences in Delft, the Netherlands as observed by persistent scatterer interferometry," in *Proc 5th Int. Workshop ERS/Envisat SAR Interferometry (FRINGE)*, Frascati, Italy, Nov. 2007, pp. 1–6.
[47] P. Dheenathayalan, M. C. Cuenca, and R. F. Hanssen, "Different approaches for psi target characterization for monitoring urban infrastructure," in *Proc. 8th Int. Workshop Adv. Sci. Appl. SAR Interferometry (FRINGE)*, Frascati, Italy, Sep. 2011, p. 8.
[48] A. A. Marques, P. Dheenathayalan, R. F. Hanssen, J. Vreeburg, and L. Rietveld, "Pipe failure predictions in drinking water systems using satellite observations," *Struct. Infrastruct. Eng.*, vol. 11, no. 8, pp. 1102–1111, 2014.

Prabu Dheenathayalan (M'08) received the B.E. (sandwich) degree in electrical and electronics from the PSG College of Technology, Coimbatore, India, in 2005, and the M.Sc. degree in information and communication engineering from the Karlsruhe Institute of Technology, Karlsruhe, Germany, in 2009. He is currently pursuing the Ph.D. degree with the Department of Geoscience and Remote Sensing, Delft University of Technology, Delft, The Netherlands.

He was with Honeywell Technology Solutions, Bengaluru, India, from 2005 to 2007. During his master's degree, he was with Harman Becker Automotive Systems GmbH, Karlsbad, Germany, and the German Aerospace Center (DLR), Weßling, Germany. He is also a Researcher with the Department of Geoscience and Remote Sensing, Delft University of Technology. He holds two granted patents. His research interests include remote sensing, SAR interferometry, and image/signal processing.

David Small (S'85–M'98) received the B.A.Sc. degree in systems design engineering from the University of Waterloo, Waterloo, ON, Canada, in 1988, the M.A.Sc. degree in electrical engineering from The University of British Columbia, Vancouver, BC, Canada, in 1991, and the Ph.D. degree from Remote Sensing Laboratories, Department of Geography, University of Zürich, Zürich, Switzerland, in 1998. In his Ph.D. thesis, he developed a processing chain for generating digital elevation models from repeat-pass ERS data.

In addition to geometric and radiometric calibration of SAR imagery, applying terrain flattening to improve SAR-based wet snow mapping, he is involved in SAR polarimetry and interferometry. He currently leads the SARLab, Remote Sensing Laboratories, University of Zürich, together with D. Henke.

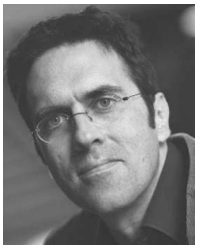

Ramon F. Hanssen (M'04–SM'15) received the M.Sc. degree in geodetic engineering and the Ph.D. degree *(cum laude)* from the Delft University of Technology, Delft, The Netherlands, in 1993 and 2001, respectively.

He was with the International Institute for Aerospace Survey and Earth Science (ITC), Stuttgart University, Stuttgart, Germany; the German Aerospace Center (DLR), Weßling, Germany; Stanford University, Stanford, CA, USA, as a Fulbright Fellow; and the Scripps Institution of Oceanography, University of California at San Diego, La Jolla, CA, USA, involved in microwave remote sensing, radar interferometry, signal processing, and geophysical application development. Since 2008, he has been an Antoni van Leeuwenhoek Professor in earth observation with the Delft University of Technology, where he has been leading the research group on mathematical geodesy and positioning since 2009. He has authored a textbook on radar interferometry.